Electronic Supplementary Material (ESI) for Physical Chemistry Chemical Physics.

SUPPLEMENTARY MATERIAL

Theoretical predictions of phase stability for orthorhombic and hexagonal ternary MAB phases

Adam Carlsson*, Johanna Rosen, Martin Dahlqvist*

Materials Design, Department of Physics, Chemistry and Biology (IFM),
Linköping University, SE-581 83 Linköping, Sweden

Corresponding authors: adam.carlsson@liu.se, martin.dahlqvist@liu.se

Magnetic spin configurations

The magnetic configurations considered span all the nonequivalent configurations within the unit cell of each composition as well as a few antiferromagnetic configurations beyond the unit cell. The configurations for the orthorhombic symmetries are found in Figure S1-S2 whereas the configurations for the hexagonal symmetries are found in Figure S3-S4. The colours of the metals indicate its spin where the blue colour represents a positive spin-polarization and red negative. The grey atoms represent the A-elements and green the boron. The energy of each phase included within the study was the lowest energy obtained from the considered spin-configurations which are presented in Table S1.

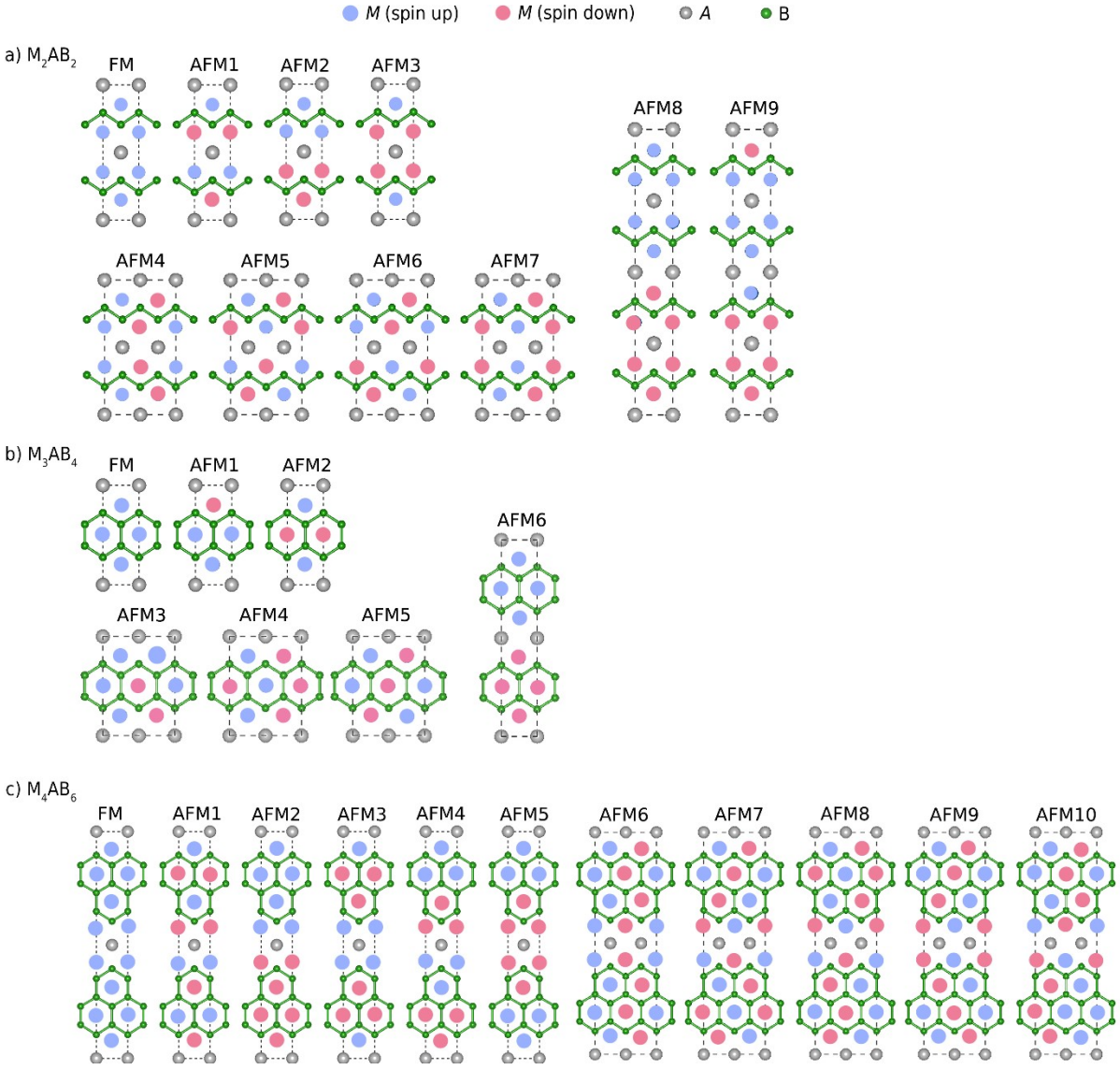

Figure S1. The magnetic spin-polarization of the orthorhombic $^{M_{n+1}AB_{2n}}$ compositions in which panel a) demonstrates ^{M_2AB_2}, b) ^{M_3AB_4} and c) ^{M_4AB_6}. The coloured atoms indicate the magnetic spin-polarization for the metal M: blue positive and red negative spin-polarization. Gray and green atoms represent A and B atoms, respectively.

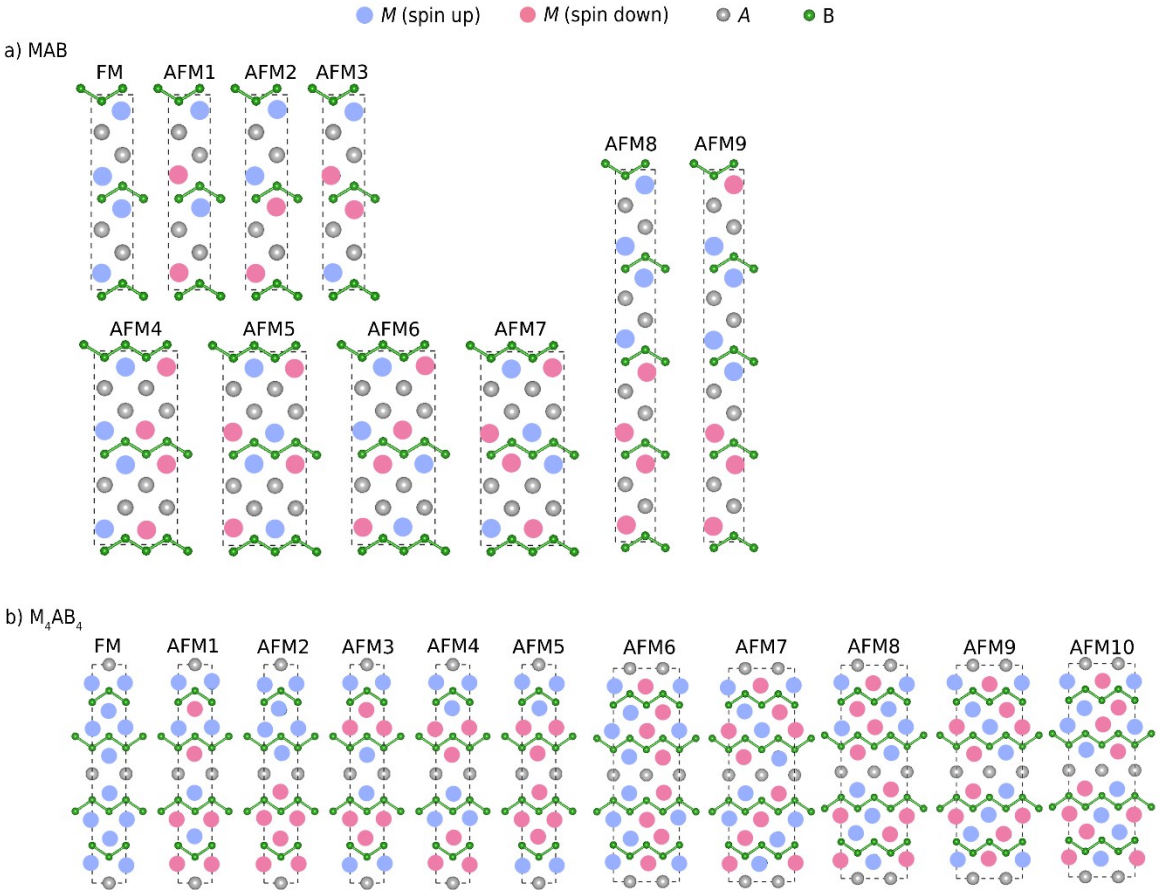

Figure S2. The magnetic spin-polarization of the orthorhombic double layered symmetries in which panel a) demonstrates MAB and b) M_4AB_4. The coloured atoms indicate the magnetic spin-polarization for the metal *M*: blue positive and red negative spin-polarization. Gray and green atoms represent *A* and B atoms, respectively.

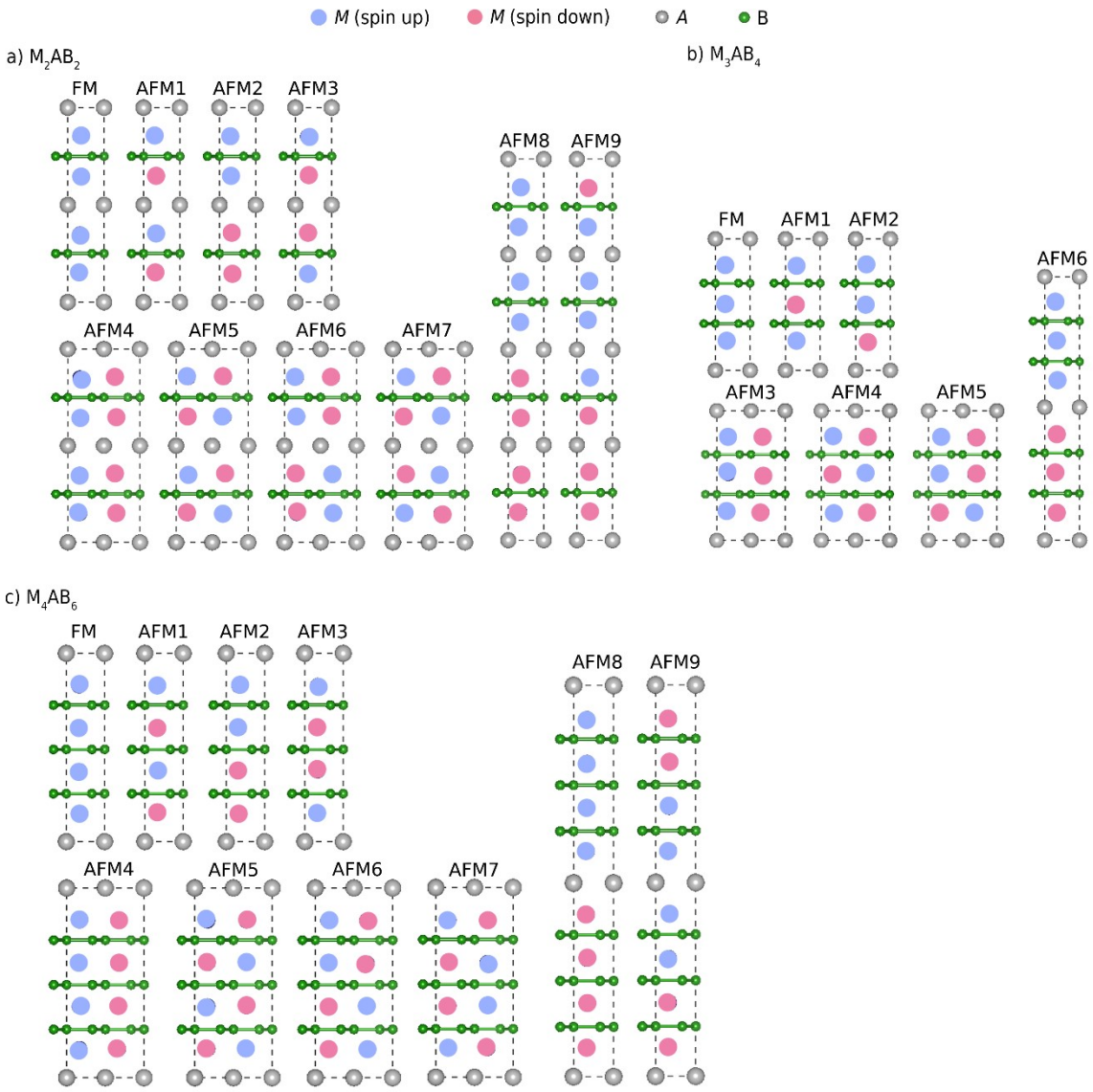

Figure S3. The magnetic spin-polarization of the hexagonal $^{M_{n+1}AB_{2n}}$ compositions in which panel a) demonstrates ^{M_2AB_2}, b) ^{M_3AB_4} and c) ^{M_4AB_6}. The coloured atoms indicate the magnetic spin-polarization for the metal *M*: blue positive and red negative spin-polarization. Gray and green atoms represent *A* and B atoms, respectively.

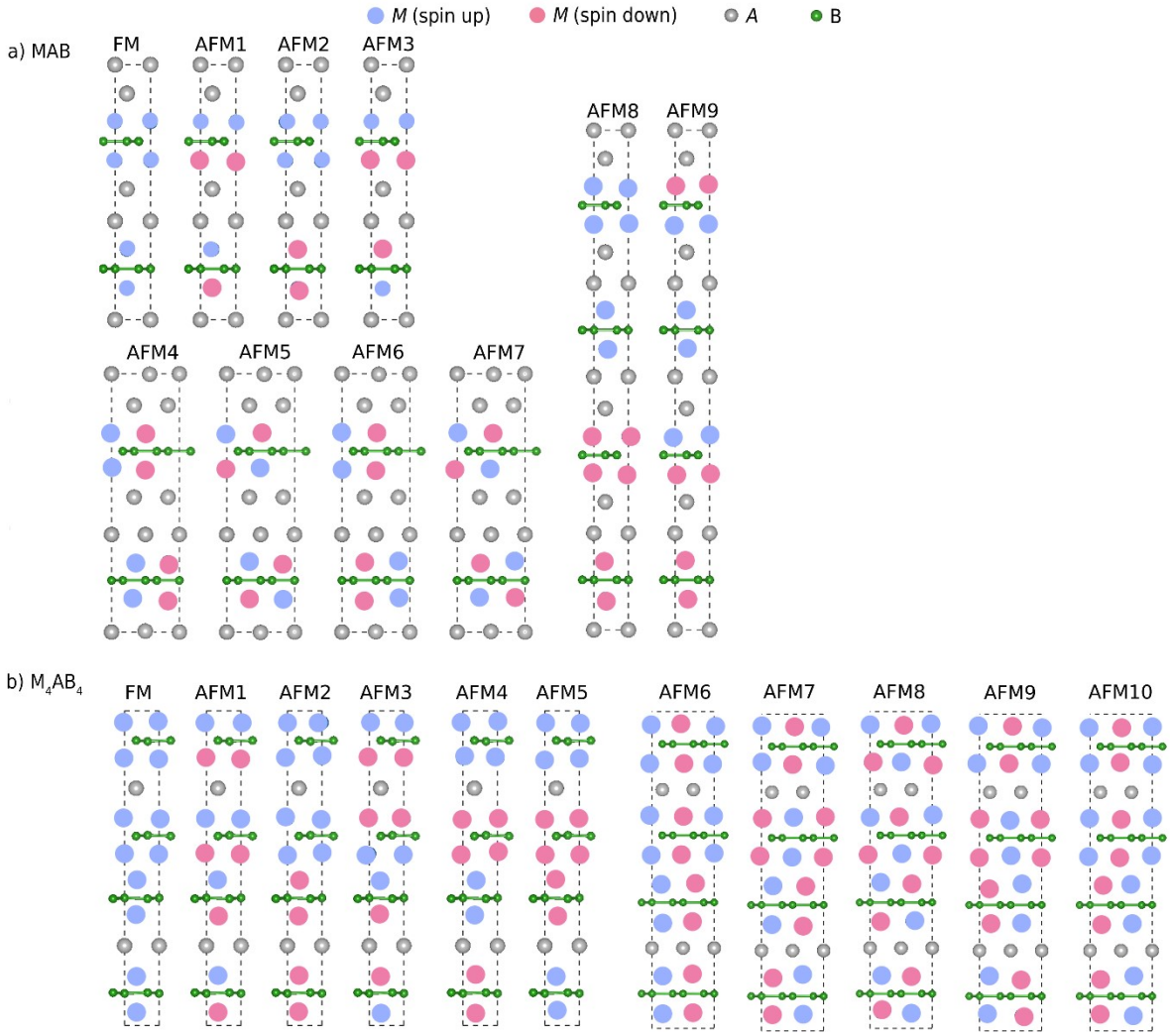

Figure S4. The magnetic spin-polarization of the hexagonal $^{M_{n+1}AB_{2n}}$ compositions in which panel a) demonstrates ^{M_2AB_2}, b) ^{M_3AB_4} and c) ^{M_4AB_6}. The coloured atoms indicate the magnetic spin-polarization for the metal *M*: blue positive and red negative spin-polarization. Gray and green atoms represent *A* and B atoms, respectively.

The majority of the magnetic phases (43 out of 60) of lowest energy favours a AFM spin configuration. In Table S1, the lowest spin configuration is demonstrated with notations defined in Figure S1 to S4. The initial index represents the preferred symmetry being either *h* or *o*, representing hexagonal or orthorhombic, respectively.

Table S1. The lowest energy spin configuration with notations from Figure S1-4. The initial letter (either *o* or *h*) represents the lowest energy symmetry, either orthorhombic (*o*) or hexagonal (*h*), respectively. NM represent a nonmagnetic configuration of lowest energy.

A	*M*	M_2AB_2	M_3AB_4	M_4AB_6	*MA*B	M_4AB_4
Al	Cr	*o*AFM2	*o*AFM4	*o*FM	*o*AM5	*o*AFM10
	Mn	*o*AFM4	*o*AFM6	*o*AFM1	*o*FM	*o*AFM3
	Fe	*o*AFM4	*o*FM	*o*AFM1	*o*AFM4	*o*AFM5
	Co	*o*FM	*o*AFM6	*o*AFM7	*o*AFM8	*o*AFM8
Ga	Cr	*h*AFM2	*h*FM	*h*NM	*h*FM	*o*AFM7
	Mn	*h*AFM3	*h*AFM1	*h*AFM2	*h*FM	*o*AFM3
	Fe	*h*AFM2	*h*AFM6	*h*FM	*h*AFM2	*o*AFM5
	Co	*h*AFM4	*h*AFM6	*h*N*M*	*h*AFM7	*o*FM
In	Cr	*h*AFM3	*o*AFM4	*h*FM	*h*AFM1	*o*AFM8
	Mn	*h*AFM3	*h*AFM1	*h*AFM1	*h*AFM1	*o*AFM1
	Fe	*h*AFM2	*h*AFM6	*h*AFM7	*h*AFM1	*o*AFM3
	Co	*h*AFM7	*h*AFM3	*h*FM	*h*AFM8	*o*AFM6

Convergence of k-point density and cut of energy

The VASP settings are motivated by converging the formation enthalpy of a set of phases, namely Ti_2InB_2, Nb_3GaB_4, Mo_4AlB_4 and WAlB. The phases were selected to cover a handful of experimentally synthesized and/or metastable phases in which A = Al, In and Ga. The considered equilibrium simplexes are denoted in table S2 and were calculated using the same settings.

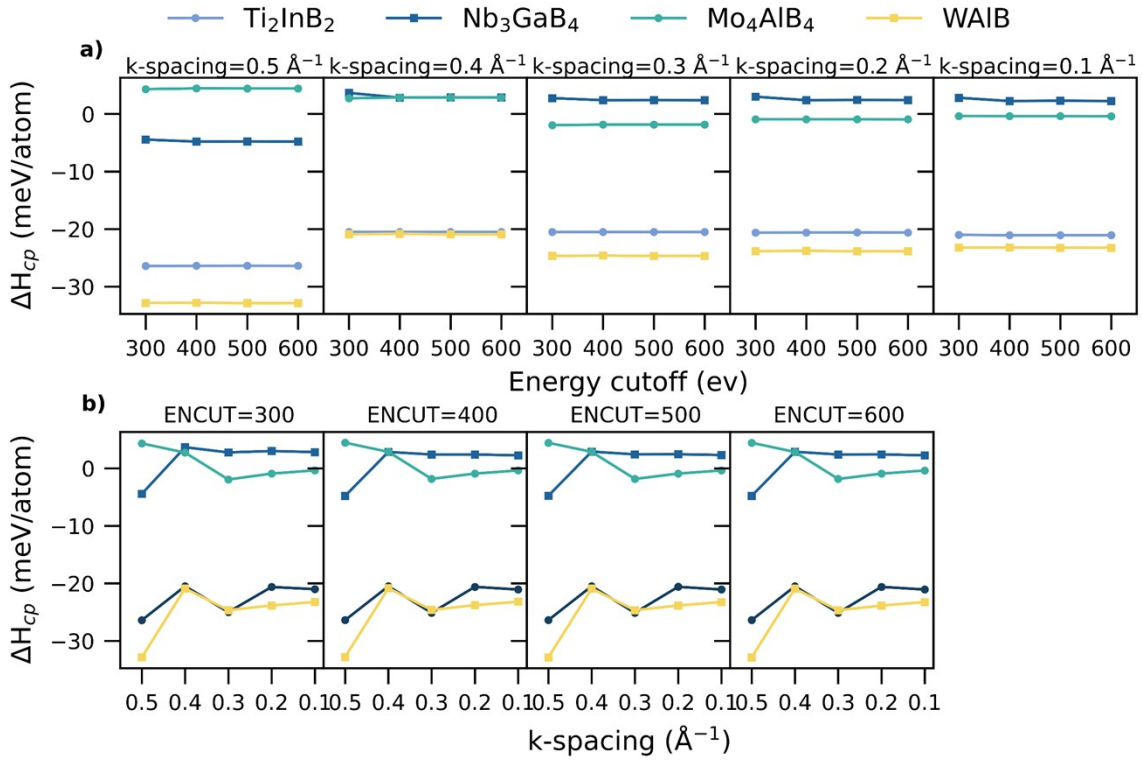

Figure S5. Convergence of formation enthalpy as a function of (a) the cutoff energy for various k-spacings, and (b) k-spacing, for various cutoff energies, for a set of considered phases; Ti_2InB_2, Nb_3GaB_4, Mo_4AlB_4 and WAlB.

The k-spacing density is according to Figure S5 the more crucial VASP setting compared to the cutoff energy. Figure S5a shows very little variation as the cutoff energy is increased while the k-point density is fixed. However, Figure S5b demonstrates significantly more variation as the k-spacing density is reduced for a fixed cutoff energy. From Figure 5 we concluded that a k-spacing density less than 0.2, independent of cutoff energy, is sufficient for required accuracy within 1 meV/atom

Information for considered crystal structures

Table S2. The crystal structure parameters for the $M_{n+1}AB_{2n}$ compositions (M_2AB_2, M_3AB_4, M_4AB_4).

Compound	Space group	Element	Wyckoff position	Atomic position	z of the lowest energy phase from Figure 3
M_2AB_2	$P\bar{6}m2$(187)	M	2i	(2/3, 1/3, z_M)	(2/3, 1/3, 0.3)
		A	1a	(0 0 0)	(0 0 0)
		B1	1d	(1/3, 2/3, z_B)	(1/3, 2/3, 1/2)
		B2	1b	(0, 0, z_B)	(0, 0, 1/2)
	Cmcm (65)	M	4j	(0, 1/2, z_M)	(0, 1/2, 0.35)
		A	2a	(0, 0, 0)	(0, 0, 0)
		B	4i	(0, 0, z_B)	(0, 0, 0.21)
M_3AB_4	$P\bar{6}m2$ (187)	M1	2i	(2/3, 1/3, z_M)	(2/3, 1/3, 0.21)
		M2	1f	(2/3, 1/3, 0.5)	(2/3, 1/3, 0.5)
		A	1a	(0,0,0)	(0,0,0)
		B1	2h	(1/3, 2/3, z_B)	(1/3, 2/3, 0.35)
		B2	2g	(0, 0, z_B)	(0, 0, 0.35)
	Pmmm (47)	M1	2r	(0, 1/2, z_{M1})	(0, 1/2, 0.30)
		M2	1a	(0, 0, 0)	(0, 0, 0)
		A	1d	(1/2, 0, 1/2)	(1/2, 0, 1/2)
		B1	2s	(1/2, 0, z_{B1})	(1/2, 0, 0.22)
		B2	2t	(1/2, 1/2, z_{B2})	(1/2, 1/2, 0.11)
M_4AB_6	$P\bar{6}m2$ (187)	M1	2i	(2/3, 1/3, z_{M1})	(2/3, 1/3, 0.16)
		M2	2i	(2/3, 1/3, z_{M2})	(2/3, 1/3,0.39)
		A	1a	(0, 0, 0)	(0, 0, 0)
		B1	2h	(1/3, 2/3, z_{B1})	(1/3, 2/3, 0.26)
		B2	2h	(0, 0, z_{B1})	(0, 0, 0.26)
		B3	1d	(1/3, 2/3, z_{B2})	(1/3, 2/3, 0.5)
		B4	1b	(0, 0, z_{B2})	(0, 0, 0.5)
	Cmmm (65)	M1	4j	(0, 1/2, z_{M1})	(0, 1/2, 0.81)
		M2	4j	(0, 1/2, z_{M2})	(0, 1/2, 0.58)
		A	4a	(0, 0, 0)	(0, 0, 0)
		B1	4i	(0, 0, z_{B1})	(0, 0, 0.10)
		B2	4i	(0, 0, z_{B2})	(0, 0, 0.27)
		B3	4i	(0, 0, z_{B3})	(0, 0, 0.35)

Table S3. The crystal structure parameters for the double layered compositions (MAB, M_4AB_4).

Compound	Space group	Element	Wyckoff position	Atomic position	z of lowest energy phase from Figure 4
MAB	$P\bar{6}_3/mmc$ (194)	M	4f	(1/3, 2/3, z_M)	(1/3, 2/3, 0.67)
		A	4f	(1/3, 2/3, z_A)	(1/3, 2/3, 0)
		B1	2b	(0, 0, z_B)	(0, 0, 0.25)
		B2	2c	(1/3, 2/3, z_B)	(1/3, 2/3, 0.25)
	Cmcm (63)	M	4c	(0, 1/4, z_M)	(0, 1/4, 0.58)
		A	4c	(0, 1/4, z_A)	(0, 1/4, 0.81)
		B	4c	(0, 1/4, z_B)	(0, 1/4, 0)
M_4AB_4	$P\bar{6}m2$ (187)	M1	2i	(2/3, 1/3, z_{M1})	(2/3, 1/3, 0.30)
		M2	2g	(0, 0, z_{M2})	(0, 0, 0.80)
		M3	2i	(2/3, 1/3, z_{M3})	(2/3, 1/3, 0.59)
		M4	2g	(0, 0, z_{M4})	(0, 0, 0.09)
		A1	1b	(0, 0, z_{A1})	(0, 0, 0.5)
		A2	1e	(2/3, 1/3, z_{A2})	(1/3, 2/3, 0)
		B1	2h	(1/3, 2/3, z_{B1})	(1/3, 2/3, 0.36)
		B2	2h	(0, 0, z_{B1})	(1/3, 2/3, 0.86)
		B3	2g	(0, 0, z_{B2})	(0, 0, 0.36)
		B4	2i	(2/3, 1/3, z_{B2})	(2/3, 1/3, 0.86)
	Immm (71)	M1	4g	(0, 0, z_{M1})	(0, 0, 0.30)
		M2	4h	(0, 1/2, z_{M2})	(0, 1/2,0.09)
		A	2b	(0, 1/2, 1/2)	(0, 1/2, 1/2)
		B1	4h	(0, 1/2, z_{B1})	(0, 1/2, 0.38)
		B2	4g	(0, 0, z_{B2})	(0, 0, 0.17)

Additional hypothetical crystal structures

Additional structures which were included within the stability analysis for the hypothetical double layered structures of *MA*B and M_4AB_4. The crystal structure parameters are of the structures within Figure S6 are found in Table S3. The blue represents a metal atom, gray an *A*-element and green being boron.

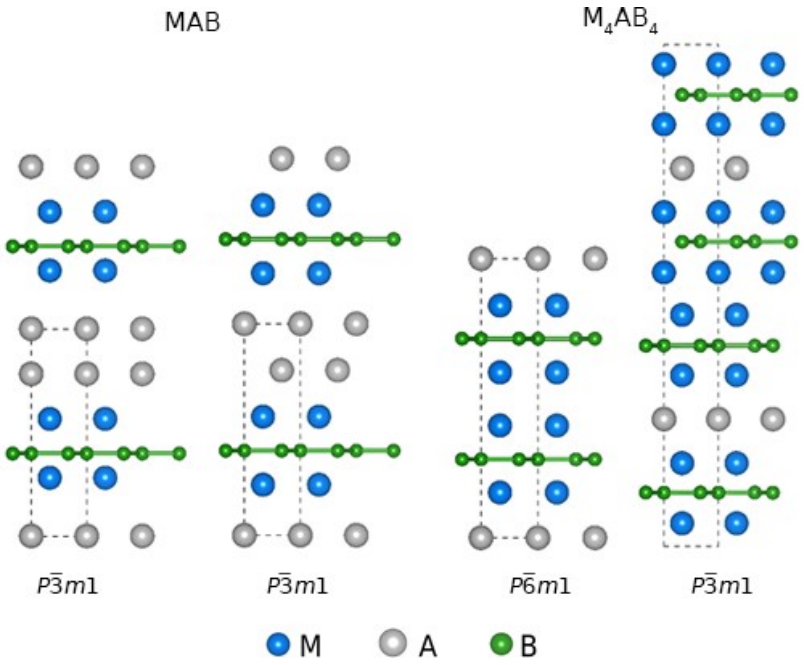

Figure S6. Additional manually designed double layered crystal structures inspired by the orthogonal counterparts. Blue, gray and green atoms represent *M*, *A,* and B atoms, respectively.

Table S4. Additional hypothetical structures which were included within the stability analysis. The crystal structures are demonstrated in Figure S6.

Compound	Space group	Element	Wyckoff position	Atomic position	z of lowest energy phase
MAB	$P\bar{3}m1$ (164)	M	2c	(0, 0, z_M)	(0, 0, 0.33)
		A	2d	(1/3, 2/3, z_A)	(1/3, 2/3, 0.12)
		B	2d	(1/3, 2/3, z_B)	(1/3, 2/3, 0.5)
	$P\bar{3}m1$ (156)	M1	1c	(2/3, 1/3, z_{M1})	(2/3, 1/3, 0.28)
		M2	1c	(2/3, 1/3, z_{M2})	(2/3, 1/3, 0.52)
		A1	1a	(0, 0, z_{A1})	(0, 0, 0.13)
		A2	1a	(0, 0, z_{A2})	(0, 0, 0.67)
		B1	1a	(0, 0, z_{B1})	(0, 0, 0.4)
		B2	1b	(1/3, 2/3, z_{B2})	(1/3, 2/3, 0.4)
M_4AB_4	$P\bar{3}m1$ (156)	M1	1c	(2/3, 1/3, z_{M1})	(2/3, 1/3, 0.05)
		M2	1b	(1/3, 2/3, z_{M2})	(1/3, 2/3, 0.55)
		M3	1c	(2/3, 1/3, z_{M3})	(2/3, 1/3, 0.34)
		M4	1b	(1/3, 2/3, z_{M4})	(1/3, 2/3, 0.84)
		M5	1c	(2/3, 1/3, z_{M5})	(2/3, 1/3, 0.17)
		M6	1b	(1/3, 2/3, z_{M6})	(1/3, 2/3, 0.67)
		M7	1c	(2/3, 1/3, z_{M7})	(2/3, 1/3, 0.47)
		M8	1b	(1/3, 2/3, z_{M8})	(1/3, 2/3, -0.04)
		A1	1a	(0, 0, z_{A1})	(0, 0, 0.25)
		A2	1c	(2/3, 1/3, z_{A2})	(2/3, 1/3, 0.75)
		B1	1b	(1/3, 2/3, z_{B1})	(1/3, 2/3, 0.11)
		B2	1a	(0, 0, z_{B2})	(0, 0, 0.61)
		B3	1a	(0, 0, z_{B3})	(0, 0, 0.11)
		B4	1c	(2/3, 1/3, z_{B4})	(2/3, 1/3, 0.61)
		B5	1b	(1/3, 2/3, z_{B5})	(1/3, 2/3, 0.40)
		B6	1a	(0, 0, z_{B6})	(0, 0, 0.90)
		B7	1a	(0, 0, z_{B7})	(0, 0, 0.40)
		B8	1c	(2/3, 1/3, z_{B8})	(2/3, 1/3, -0.10)
	$P\bar{6}m1$ (187)	M1	2i	(2/3, 1/3, z_{M1})	(2/3, 1/3, 0.16)
		M2	2i	(2/3, 1/3, z_{M2})	(2/3, 1/3, 0.60)
		A	1a	(0, 0, z_A)	(0, 0, 0)
		B1	2h	(1/3, 2/3, z_{B1})	(1/3, 2/3, 0.28)
		B2	2g	(0, 0, z_{B2})	(0, 0, 0.28)

Set of most competing phases

Table S5. Equilibrium simplex (set of most competing phases) for the considered $M_{n+1}AB_{2n}$ phases (M_2AB_2, M_3AB_4, M_4AB_6) herein used when determining the stability based on the formation enthalpy.

	Equilibrium simplex of $M_{n+1}AB_{2n}$ phases		
Metals	M_2AlB_2	M_3AlB_4	M_4AlB_6
Sc	ScB_2, ScAl	ScB_2, ScAl	ScB_2, ScAl
Y	YB_2, Y_2Al, YAl_2	YB_2, Y_2Al, YAl_2	YB_2, Y_2Al, YAl_2
Ti	TiAl, TiB_2	TiB_2, TiAl	TiB_2, TIAl
Zr	ZrB_2, Zr_2Al_3, Zr_4Al_3	ZrB_2, Zr_2Al_3, Zr_4Al_3	ZrB_2, Zr_2Al_3, Zr_4Al_3
Hf	HfB_2, $HfAl_2$, Hf_4Al_3	HfB_2, $HfAl_2$, Hf_4Al_3	HfB_2, $HfAl_2$, Hf_4Al_3
V	V_5B_6, VAl_3	V_3B_4, Al	V_2B_3, Al
Nb	NbB, Nb_3B_4, $NbAl_3$	Nb_2B_3, NbAl3	Nb_2B_3, NbB_2, $NbAl_3$
Ta	TaB, Ta_3B_4, $TaAl_3$	Ta_3B_4, Al	Ta_3B_4, TaB_2, Al
Cr	CrAlB, Cr_4AlB_4	Cr_2AlB_2, CrB_2	CrB_2, Cr_2AlB_2
Mo	MoAlB, Mo_4AlB_4	MoB_2, MoAlB, Mo_4AlB_4	MoB_2, MoAlB, MoB
W	WAlB, WB	WAlB, WB, WB_2	WB_2, WAlB, WB
Mn	MnB, MnB_4, Mn_4Al_{11}	Mn_2AlB_2, MnB, MnB_4	MnB, Mn_2AlB_2, MnB_4
Fe	FeAlB, α-FeB	Fe_2AlB_2, α-FeB, B	α-FeB, B, Fe_2AlB_2
Co	CoB, B, CoAl	CoB, B, CoAl	CoB, B, CoAl
	M_2GaB_2	M_3GaB_4	M_4GaB_6
Sc	ScB_2, $ScGa_2$, $Sc_{11}Ga_{10}$	ScB_2, $ScGa_2$, $Sc_{11}Ga_{10}$	ScB_2, $ScGa_2$, $Sc_{11}Ga_{10}$
Y	YB_2, YGa_2, Y_5Ga_3	YB_2, YGa_2, Y_5Ga_3	YB_2, YGa_2, Y_5Ga_3
Ti	TiB_2, TiGa	TiB_2, TiGa	TiB_2, TiGa
Zr	ZrB_2, ZrGa	ZrB_2, ZrGa	ZrB_2, ZrGa
Hf	HfB_2, HfGa	HfB_2, HfGa	HfB_2, HfGa
V	VB, V_5B_6, V_8Ga_{41}	V_3B_4, Ga	V_2B_3, Ga
Nb	NbB, Nb_3B_4, Nb_5Ga_{13}	Nb_2B_3, Ga, Nb_5Ga_{13}	Nb_2B_3, Ga
Ta	TaB, Ga	Ga, Ta_3B_4	Ga, TaB_2, Ta_3B_4
Cr	CrB, Ga	CrB, CrB_2, Ga	CrB, CrB_2, Ga
Mo	MoB, MoB_2, $MoGa_4$	MoB, MoB_2, $MoGa_4$	MoB_2, MoB, $MoGa_4$
W	WB, Ga	WB, WB_2, Ga	WB_2, WB, Ga
Mn	MnB, $MnGa_4$, MnB_4	MnB, MnB_4, $MnGa_4$	MnB, MnB_4, $MnGa_4$
Fe	FeB, $FeGa_3$, B	FeB, B, $FeGa_3$	FeB, B, FeG_3
Co	CoB, Ga	CoB, Ga, B	CoB, B, Ga
	M_2InB_2	M_3InB_4	M_4InB_6
Sc	ScB_2, ScIn	ScB_2, ScIn	ScB_2, ScIn
Y	YB_2, Y_5In_3, Y_3In_5	YB_2, Y_5In_3, Y_3In_5	YB_2, Y_5In_3, Y_3In_5
Ti	Ti_3InB_4, TiIn	TiB_2, Ti_2InB_2	TiB_2, Ti_2InB_2
Zr	ZrB_2, ZrIn	ZrB_2, Zr_2InB_2	ZrB_2, Zr_2InB_2
Hf	Hf_3InB_4, Hf, Hf_2In_5	HfB_2, Hf_2InB_2	HfB_2, Hf_2InB_2
V	VB, In	V_3B_4, In	V_2B_3, In
Nb	NbB, In	Nb_3B_4, In	Nb_2B_3, In
Ta	TaB, In	Ta_3B_4, In	TaB_2, Ta_3B_2, In
Cr	CrB, In	CrB, CrB_2, In	CrB, CrB_2, In
Mo	MoB, In	MoB, MoB_2, In	MoB_2, MoB, In
W	WB, In	WB, WB_2, In	WB_2, WB, In
Mn	MnB, In	MnB, In, MnB_4	MnB, In, MnB_4
Fe	FeB, In	FeB, B, In	FeB, B, In
Co	CoB, In	CoB, In, B	CoB, B, In

Table S6. Equilibrium simplex (set of most competing phases) for the considered double layered phases, (MAB and M_4AB_4) herein used when determining the stability based on the formation enthalpy.

Metals	*M*AlB	M_4AlB_4
Sc	$ScAl_2$, ScB_2	ScB_2, Sc_2Al
Y	YB_2, YAl_2	YB_2, Y_2Al
Ti	$TiAl_2$, TiB_2	Ti_3B_4, TiAl
Zr	$ZrAl_2$, ZrB_2	ZrB_2, Zr_3Al, Zr_4Al_3
Hf	$HfAl_2$, HfB_2	HfB_2, Hf, HfAl
V	V_3B_4, VAl_3, Al	VB, V_5B_6. VAl_3
Nb	Nb_2B_3, $NbAl_3$	NbB, Nb_3B4, $NbAl_3$
Ta	Ta_3B_4, $TaAl_3$, Al	TaB, Ta_3B4, $TaAl_3$
Cr	Cr_2AlB_2, Al	CrB, Cr_2AlB_2
Mo	MoB_2, Mo_2AlB_2, Mo_3Al_8	MoB, MoAlB
W	WB, WB_2, WAl_5	WB, WAlB
Mn	Mn_2AlB_2, $MnAl_6$, MnB_4	MnB, Mn_2AlB_2
Fe	Fe_2AlB_2, Al	FeB, Fe_2AlB_2
Co	CoAl, B	CoB, CoAl, B
	*M*GaB	M_4GaB_4
Sc	ScB_2, $ScGa_2$	ScB_2, Sc_5Ga_3, Sc
Y	YB_2, YGa_2	YB_2, Y_5Ga_3, Y
Ti	TiB_2, $TiGa_2$	TiB_2, Ti_2Ga
Zr	$ZrGa_2$, ZrB_2	ZrB_2, Zr_2Ga
Hf	$HfGa_2$, HfB_2	HfB_2, Hf_2Ga
V	V_5B_6, V_3B_4, V_8Ga_{41}	VB, V_5B_6, V_8Ga_{41}
Nb	Nb_2B_3, Ga, Nb_5Ga_{13}	NbB, Nb_3B_4, Nb_5Ga_{13}
Ta	TaB, Ga	TaB, Ga
Cr	CrB, Ga	CrB, Ga
Mo	MoB, MoB_2, $MoGa_4$	MoB, MoB_2, $MoGa_4$
W	WB, Ga	WB, Ga
Mn	MnB, $MnGa_4$, MnB_4	MnB, $MnGa_4$, MnB_4
Fe	FeB, FeG_3, B	FeB, $FeGa_3$, B
Co	CoB, Ga	CoB, Ga
	*M*InB	M_4InB_4
Sc	ScB_2, $ScIn_2$	ScB_2, Sc_2In
Y	YB_2, Y_3In_5, YB_4	YB_2, Y_2In
Ti	TiB_2, Ti_2In_5, Ti_2InB_2	TiB, Ti_2InB_2
Zr	ZrB_2, $ZrIn_2$	ZrB_2, Zr_3In, Zr_2InB_2
Hf	HfB_2, Hf_2In_5, Hf_2InB_2	HfB_2, Hf_2InB_2, Hf
V	VB, In	VB, In
Nb	NbB, In	NbB, In
Ta	TaB, In	TaB, In
Cr	CrB, In	CrB, In
Mo	MoB, In	MoB, In
W	WB, In	WB, In
Mn	MnB, In	MnB, In
Fe	FeB, In	FeB, In
Co	CoB, In	CoB, In

Considered binary phases

Tabel S7. The considered binary phases and space group symmetries obtained from the Springer materials database.

phase	Space group	Space group	Symmetry
CrB	*oS*8	63	Orthorhombic
CrB_2	*hP*3	191	Hexagonal
VB	*oS*8	63	Orthorhombic
VB_2	*hP*3	191	Hexagonal
Ti_3B_4	*oI*14	71	Orthorhombic
TiB	*oP*8	62	Orthorhombic
TiB_2	*hP*3	191	Hexagonal
ScB_2	*hP*3	191	Hexagonal
YB_2	*hP*3	191	Hexagonal
ZrB_2	*hP*3	191	Hexagonal
Nb_3B_4	*o*/14	71	Orthorhombic
Nb_5B_6	*oS*22	65	Orthorhombic
NbB	*oS*8	63	Orthorhombic
NbB_2	*hP*3	191	Hexagonal
MoB	*oS*8	63	Orthorhombic
MoB_{12}	*hP*16	194	Hexagonal

Information of considered atomic size and electron concentration

Table S8. Considered atomic size, valence electrons and itinerant electrons for M- and A-element, used herein. Data obtained from [1, 2].

Element	Radius (Å)	Valence electrons	itinerant electrons
Sc	1.62	3	2.94
Y	1.80	3	3.15
Ti	1.47	4	1.14
Zr	1.60	4	1.49
Hf	1.59	4	1.76
V	1.35	5	0.90
Nb	1.46	5	1.32
Ta	1.46	5	1.53
Cr	1.29	6	0.92
Mo	1.39	6	1.39
W	1.39	6	1.43
Mn	1.27	7	1.05
Fe	1.26	8	1.05
Co	1.25	9	1.03
Al	1.43	3	3.01
Ga	1.40	3	3.00
In	1.58	3	3.03

Attempts to explain energy difference for different crystal symmetries

In an attempt to explain the low energy symmetry preference of $\Delta E(sym)$ we construct a set of figures in which $\Delta E(sym)$ is set as a function of $R_M - R_B$, $R_M - R_A$, R_M, $|R_M - R_A|/R_M$, VEC, $Pm - Pa$, $Pm - Pb$ and Pm. Where R_M is the metallic radii, R_A the A-element radii, R_B the boron radii, $R_M - R_A|/R_M$ is the size ratio and VEC the valence electron concentration defined as in [3]. Pm is the electron negativity of the metal, Pa of the A-element and Pb of the boron. The electronegativity values are obtained from Ref. [1, 2]. No direct conclusion may be drawn based on Figure S1 as the data points of the different A-elements are seen to be clustered together.

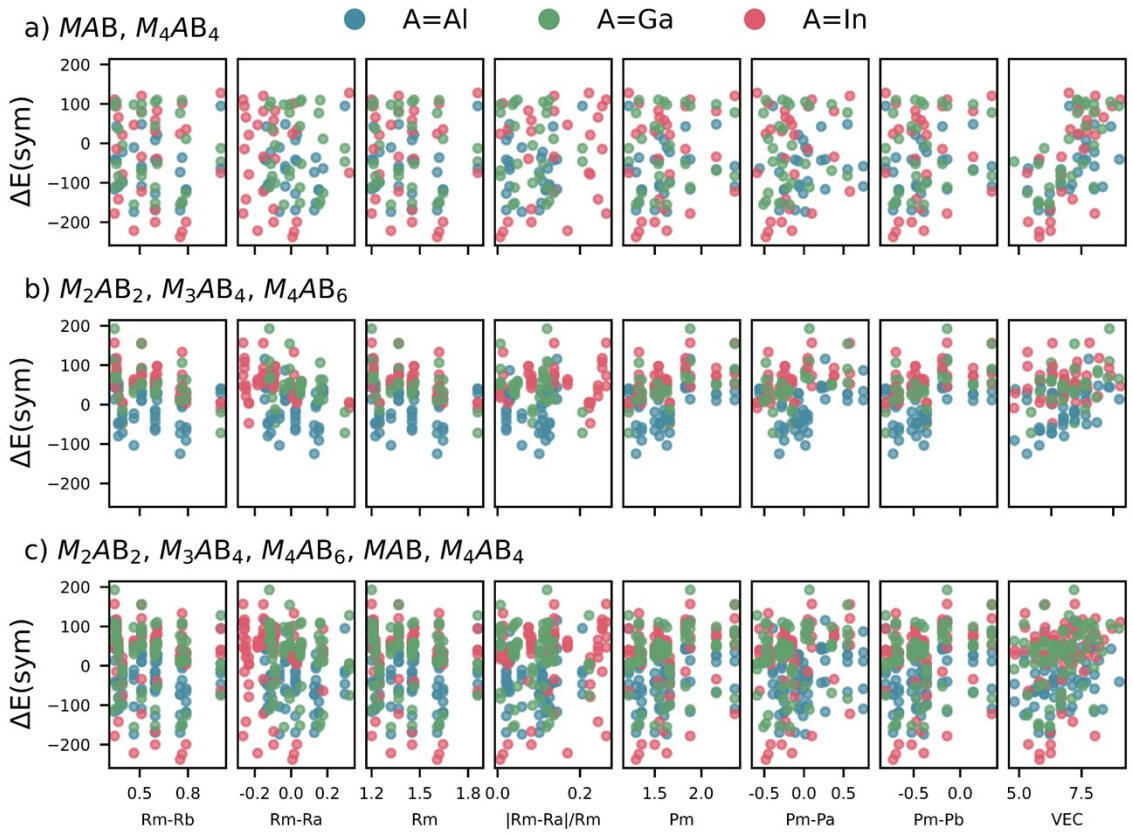

Figure S7. $\Delta E(sym)$ as a function of here in considered properties for single compositions and all compositions in an attempt to understand $\Delta E(sym)$. Panel a) demonstrates MAB, b) M_4AB_4, c) M_4AB_6, d) M_3AB_4, e) M_2AB_2 and f) all compositions grouped. The colours indicate the A-element with A = Al in blue, A = Ga in green and A = In in orange.

Bonding analysis

In an attempt to understand the symmetry preference in Figure 5, we carried out bonding analysis for a selected set of M_2AB_2 phases of both hexagonal and orthorhombic symmetry where M = Sc, Ti, V, Cr, and A = Al, In using the Local Orbital Basis Suit Towards Electronic Structure Reconstruction (LOBSTER) [4] code. Both by considering the populated bonding and anti-bonding states by studying the total density of states (DOS) and the total crystal orbital Hamiltonian population (COHP) and by considering all the induvial interactions up to 4 Å. The Cr_2AB_2 phases was considered as nonmagnetic as the energy difference between the lowest magnetic configuration and the nonmagnetic is only 7 meV / atom.

The DOS for A = Al, Figure S8, displays a peak at the fermi energy, E_f, for the hexagonal symmetry for M = Sc and a minimum for orthorhombic symmetry. As the M is further changed to Ti, V, and Cr, the E_f is seen to shift to right. The COHP displays a similar trend whereas all A = Al shows bonding states populated at the E_f except for the hexagonal Cr_2AlB_2 which displays a small antibonding contribution. The orthorhombic Cr_2AlB_2 which is the only experimentally verified phase in Figure S8 displays a well optimized DOS minima at E_f and a COHP with no excess of bonding or antibonding states. The hexagonal V_2AlB_2 displays similar features but yields a formation enthalpy of +73 meV/atom and is determined too not be stable. In relation to the symmetry preference shown in Figure 5 where Sc_2AlB_2 and Cr_2AlB_2 prefers orthorhombic symmetry while Ti_2AlB_2 and V_2AlB_2 favours hexagonal. The nature of the DOS and COHP of the most preferred symmetry displays more optimized features in the sense of a close to DOS and COHP minima at E_f.

Similarly, for the A = In phases considered in Figure S9, the hexagonal Ti_2InB_2 is the only experimentally verified phase among In-based M_2AB_2 phases. The DOS and COHP of Ti_2InB_2 demonstrates the most optimized DOS with bonding states almost filled as seen from the COHP curve. Additionally, the orthorhombic V_2InB_2 shows a prominent peak in DOS at E_f, being energetically unfavoured, and this in contrast to the hexagonal structure. This is also reflected in Figure 5 where the hexagonal V_2InB_2 is 133 meV/atom lower in energy than the orthorhombic structure. All considered M_2InB_2 phases displays a hexagonal symmetry preference in Figure 5, even Sc_2InB_2 despite being found with more unfilled bonding states above E_f than the orthorhombic structure.

In an attempt to elucidate the nature of the bonds and their possible impact on the structural preference, we looked at total and individual chemical interactions of the considered M_2AB_2 phases, shown in Figure S10 and S11. If we sum up all different interactions, the total interaction within any of the considered orthorhombic symmetries is always greater than the hexagonal structure and this independent of M or A, shown in Figure S10 as the total ICOHP/atom. If we take a look at individual interactions, there are some indications that the A-elemental interactions may fit as a descriptor for explaining the symmetry preference shown in Figure 5. Phases with A = In tend to form hexagonal structures with stronger In-In bonds (~2.5 eV) than within the orthorhombic counterpart, as shown in Figure 11. For phases with A = Al, the M-Al bonds seems to play a more significant role, especially in Sc_2AlB_2 and Cr_2AlB_2, and this is also reflected in Figure 5 where both favours orthorhombic symmetries.

Furthermore, in Figure S12 to S13 we show calculated crystal overlap Hamiltonian population (COHP) for different interactions along with total, atomic and orbital projected density of states (DOS) for orthorhombic and hexagonal symmetries of Ti_2InB_2 and Cr_2AlB_2. COHP and DOS complements each other since peaks in DOS can through COHP be assigned to be bonding (positive -COHP), non-bonding (no COHP) or antibonding (negative -COHP). A closer look at hexagonal Ti_2InB_2 reveals that the DOS peak around -1 eV can be attributed to Ti-Ti and Ti-In bonding interactions (see Figure S12ab) composed mainly of Ti $3d_{z^2}$, $3d_{xz}$ and $3d_{x^2-y^2}$, and In $5p_z$ states. This can be compared with orthorhombic Ti_2InB_2 where the peak around -1 eV can be attributed to mainly Ti-Ti interactions composed of Ti $3d_{z^2}$ while the peak around -2 eV can be attributed to Ti-In, In-In and B-Bi interactions (see Figure S13ab). Around the Fermi level, antibonding states are observed for both symmetries but is

more common in the orthorhombic structure which do have a negative impact on its energy. The location of the Fermi level in DOS also matter where it is close to a local minimum for the hexagonal symmetry which is not the case for the orthorhombic one. Overall, these differences in bonding characteristics and which orbital that contributes can be related to their structural difference with buckled layers for the orthorhombic structure while the hexagonal structure have flat layers.

A similar analysis for the orthorhombic Cr_2AlB_2 shows that the Fermi level is closer to a local minimum than for the hexagonal symmetry. Both symmetries show antibonding states around the Fermi level, mainly from Cr-Cr interactions. Further correlations are found when comparing COHP with DOS. The DOS peak around -0.5 eV for orthorhombic Cr_2AlB_2 is from Cr $3d$ and is non-bonding (no significant contribution in -pCOHP). Corresponding peak for hexagonal Cr_2AlB_2 is located just above the Fermi level and is antibonding. The details of the lower energy DOS peaks can be assigned to the symmetry difference, like for Ti_2InB_2. Overall indicating that, from an electronic and bonding perspective, the orthorhombic Cr_2AlB_2 structure is favoured over the hexagonal one.

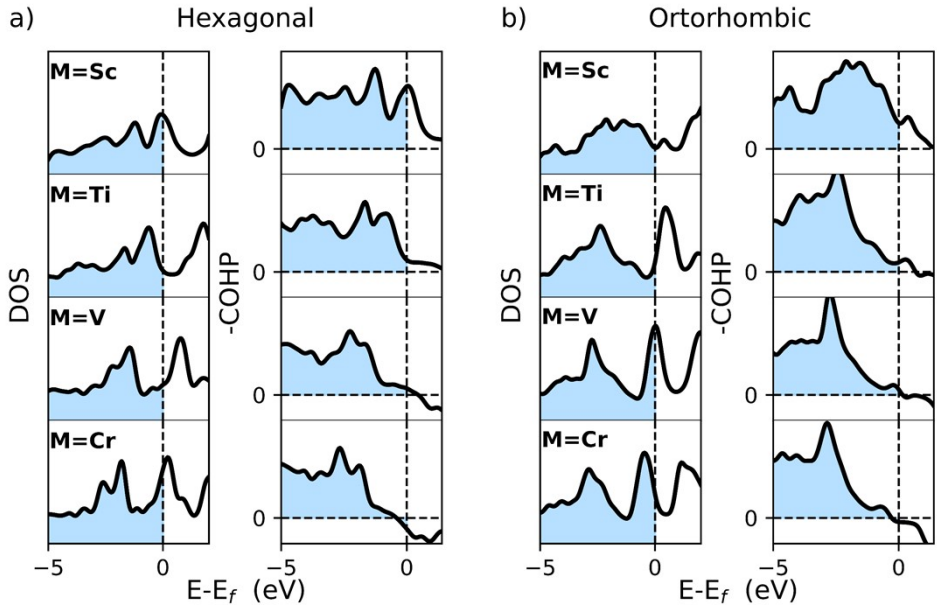

Figure S8. Calculated total DOS and -COHP for M_2AlB_2 systems of a) hexagonal and b) orthorhombic symmetry with M = Sc, Ti, V, and Cr. The dashed vertical line denotes the fermi energy

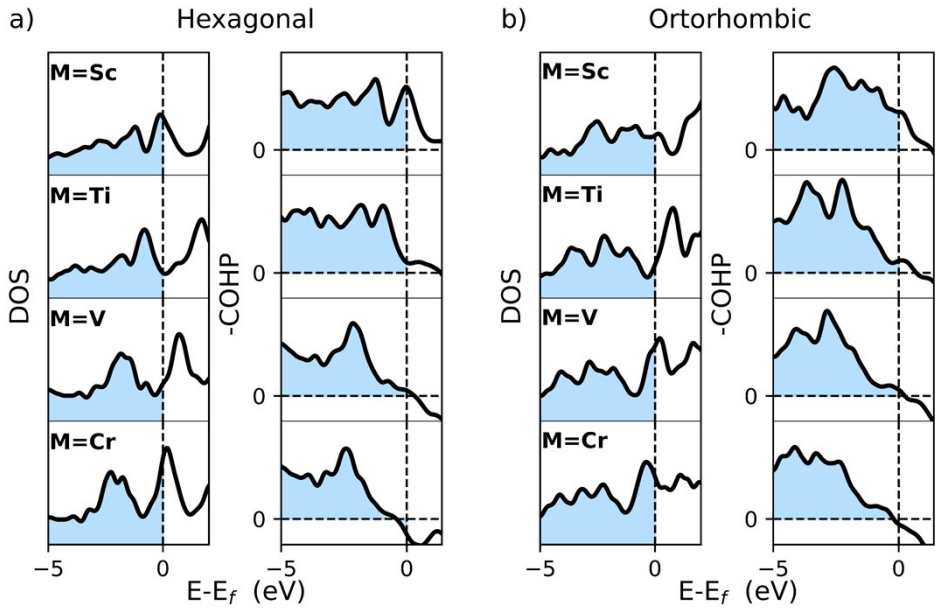

Figure S9. Calculated total DOS and -COHP for M_2InB_2 systems of a) hexagonal and b) orthorhombic symmetry with M = Sc, Ti, V, and Cr. The dashed vertical line denotes the fermi energy

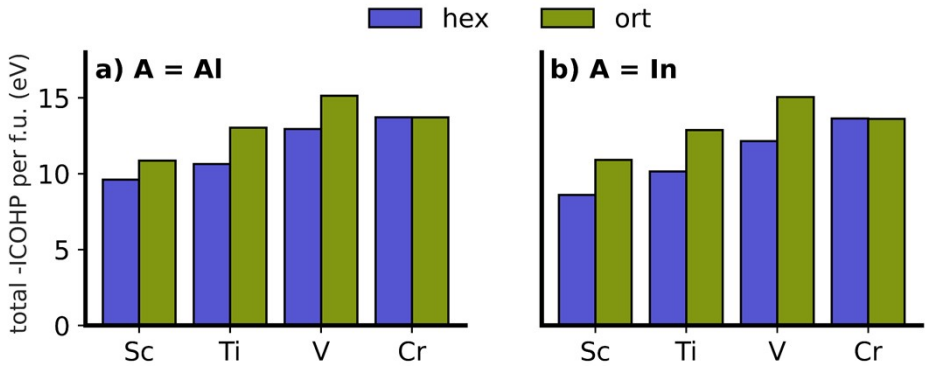

Figure S10. Ttotal -iCOHP for the selected $M_2{}^{A}B_2$ phase with M = Sc, Ti, V, and Cr where a) shows ^{A} = Al and b) ^{A} = In. Additionally, the colour denotes the symmetry with blue and red representing hexagonal and orthorhombic, respectively.

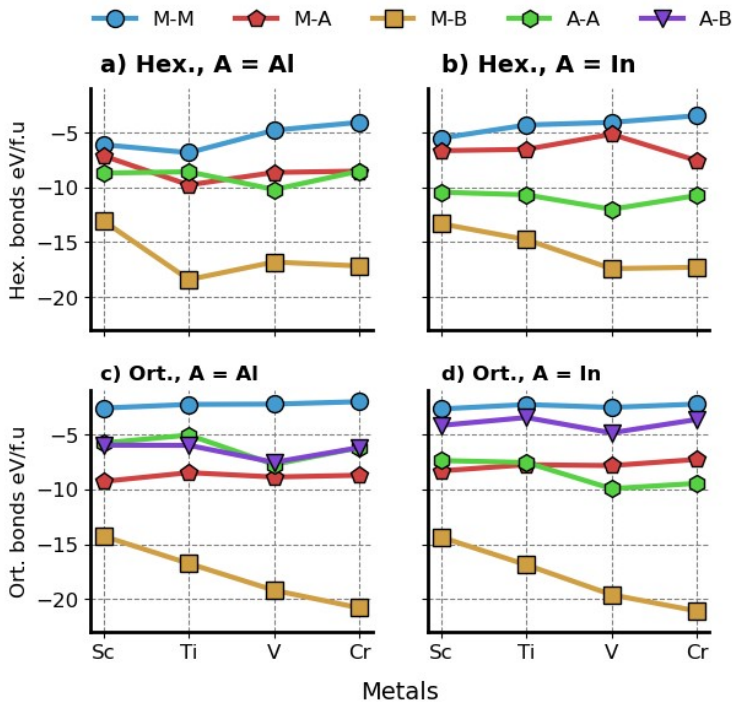

Figure S11. Contribution from individual chemical interactions for different bonds for selected M_2AB_2 systems with M = Sc, Ti, V, Cr, and A = Al, In for a) hexagonal M_2AlB_2, b) hexagonal M_2InB_2, c) orthorhombic M_2AlB_2 and d) orthorhombic M_2InB_2.

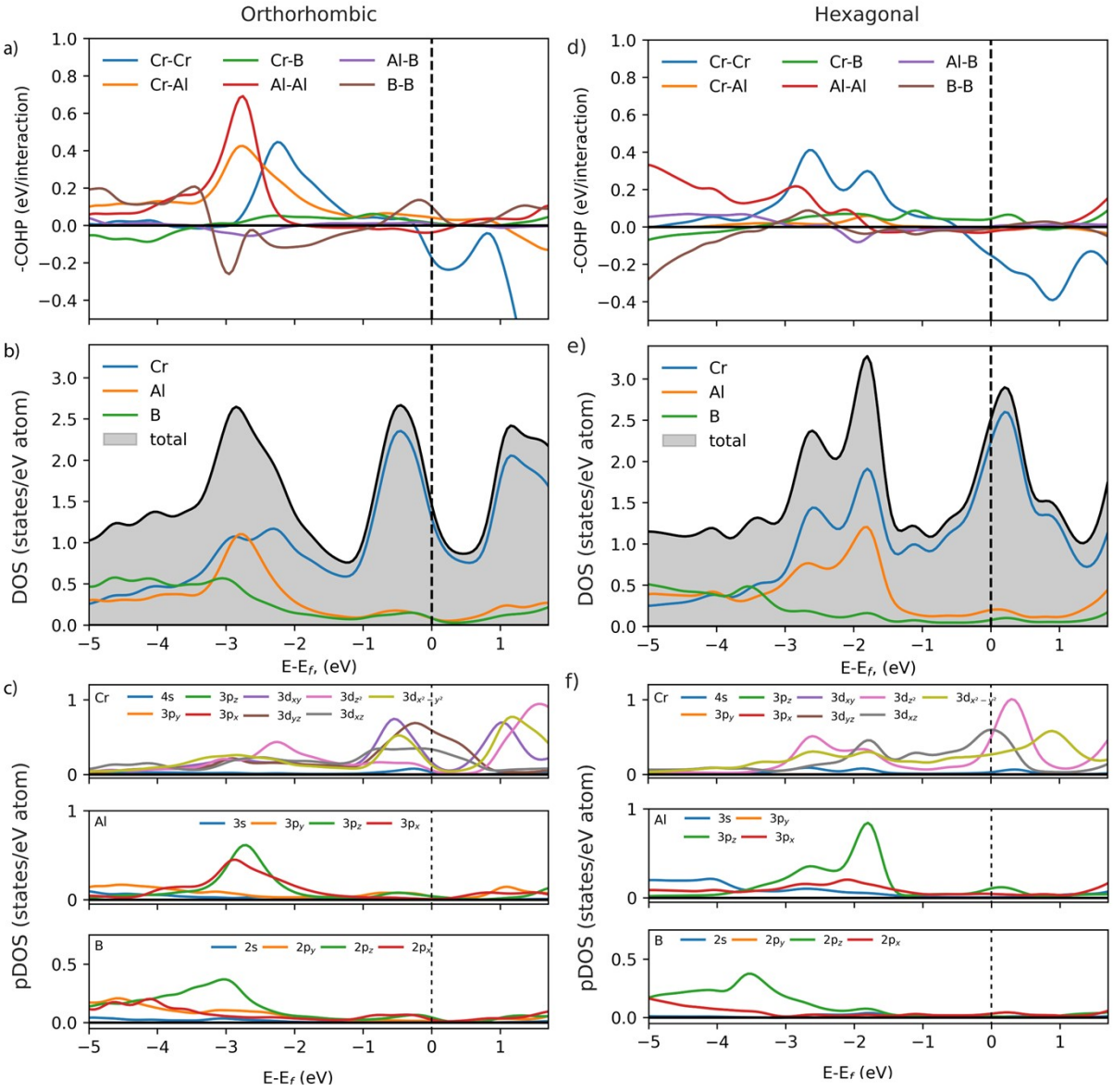

Figure S12. Calculated (a,d) crystal overlap Hamiltonian population (COHP) for different interactions, (b,e) total and atomic density of state (DOS) and (c,f) orbital projected DOS (pDOS) for (a-c) hexagonal and (d-f) orthorhombic Cr_2AlB_2.

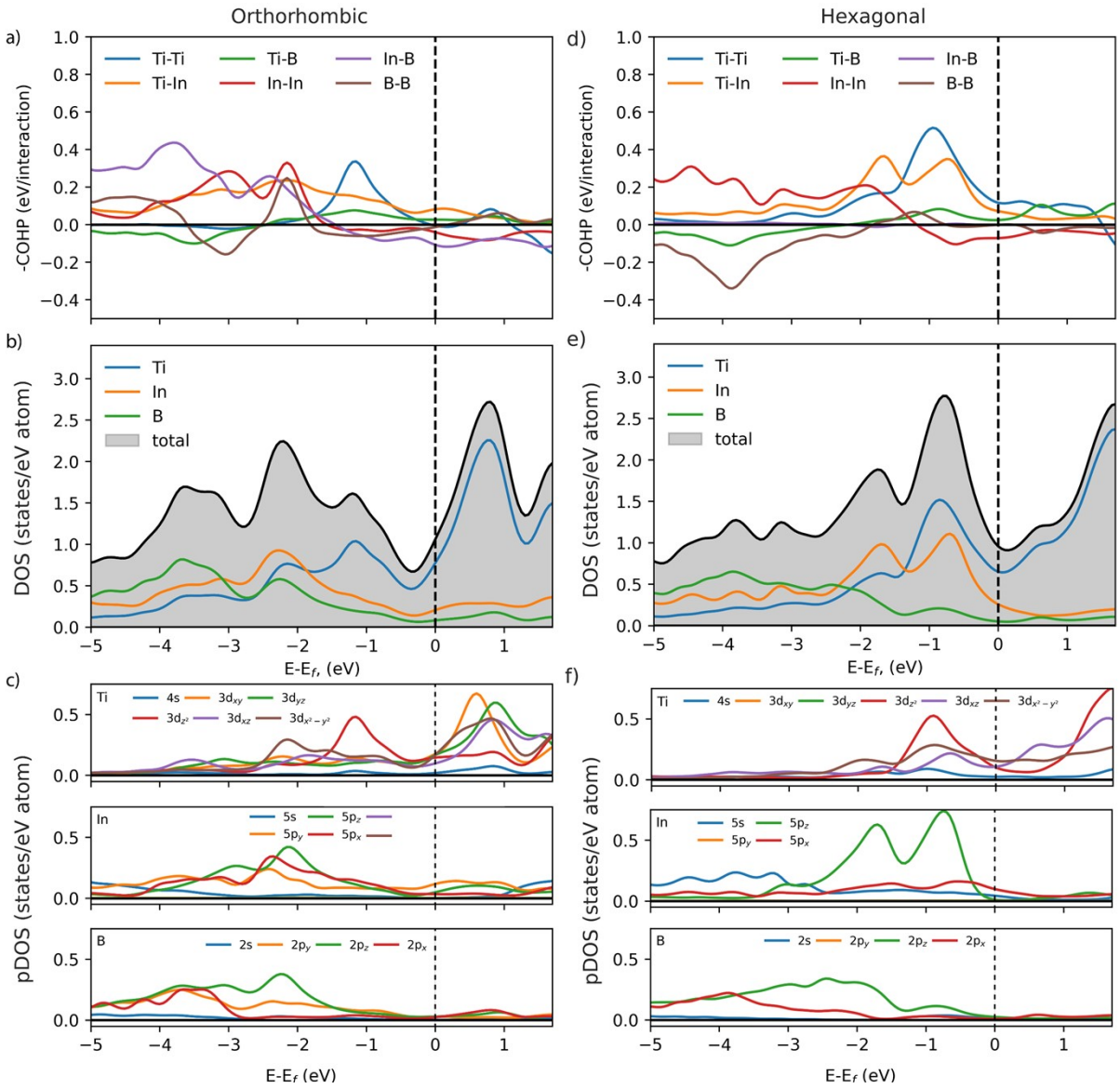

Figure S13. Calculated (a,d) crystal overlap Hamiltonian population (COHP) for different interactions, (b,e) total and atomic density of state (DOS) and (c,f) orbital projected DOS (pDOS) for (a-c) hexagonal and (d-f) orthorhombic Ti_2InB_2.

Stability in analogy with size and valence electron figures

The solid line in Figure S14demonstrates the estimated stable regions of considered M_2AX phases in Ref. [5] and the dashed represents the stable region from Ref. [3]. The lines are rigorous approximations and does not fit the considered phases herein which motivates the complexity of phase stability predictions. We argue that the only motivated cut of line which may be drawn based on Figure S1 is for phases with an atomic size ratio larger than 0.15 ($\frac{|R_M - R_A|}{R_M} > 0.15$) demonstrates formation enthalpy values which motivates nonstable phases ($\Delta H_{cp} < 50$ meV/atom). The figures below demonstrate the same features for the individual compositions considered herein in order to deceive alternative conceptions.

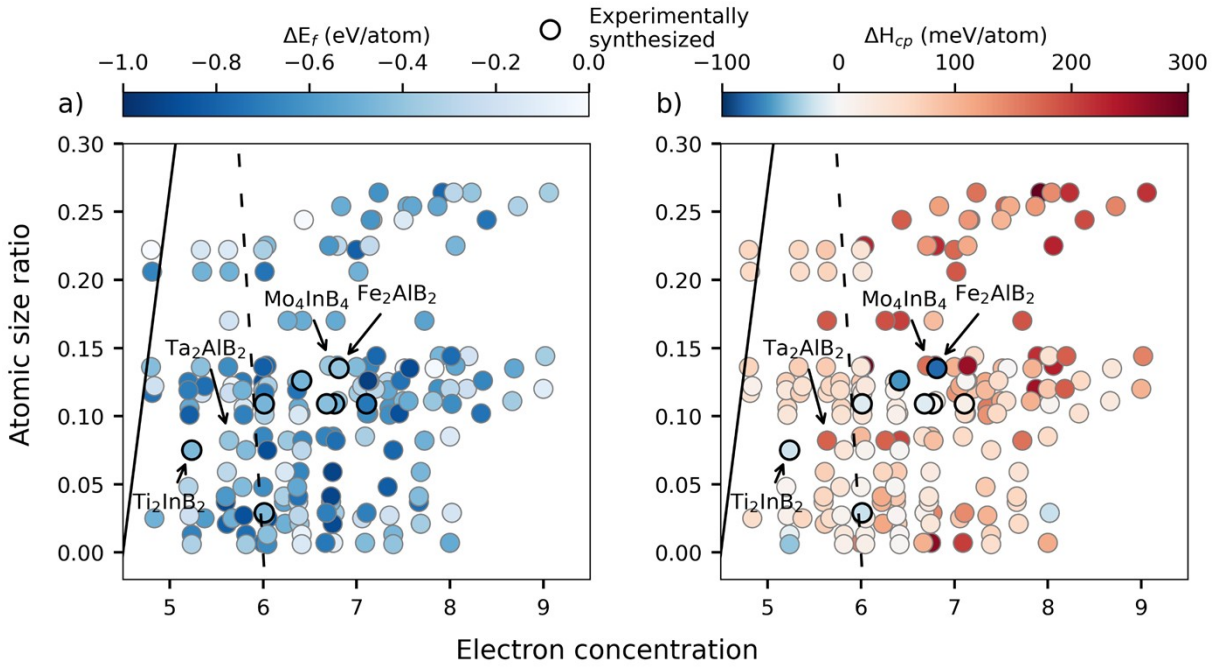

Figure S14. Atomic size ratio as a function of the electron concentration where each data point represents the lowest symmetry of a $M_xA_yB_z$ phase. The solid black line refers to the stable regions of MAX phases considered in Ref. [5] and the dashed from Ref. [3] covering stable M_4AB_4 compositions. The colour gradient in (a) and (b) is represented by the calculated ΔE_f and ΔH_{cp}, respectively. Experimentally synthesized phases are marked with a black circle.

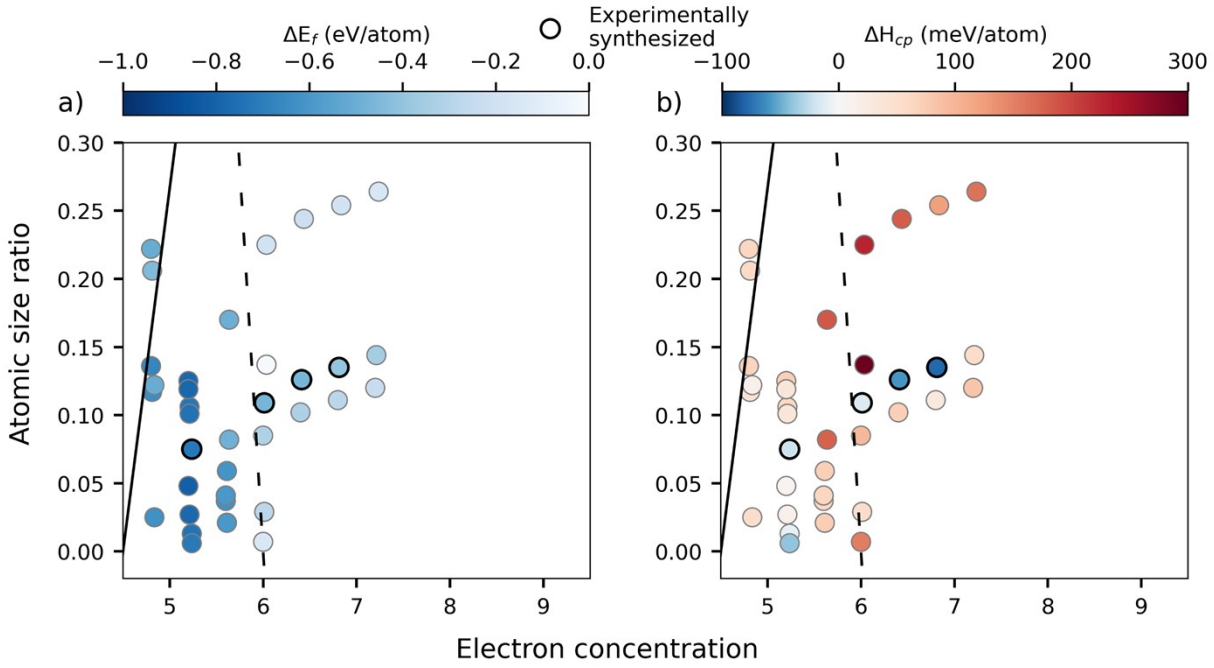

Figure S15. Atomic size ratio as a function of the electron concentration where each data point represents the lowest symmetry of a M_2AB_2 phase. The solid black line refers to the stable regions of MAX phases considered in Ref. [5] and the dashed from Ref. [3] covering stable M_2AB_2 compositions. All phases located to the left of the lines are supposedly stable. (b) and (c) The colour gradient in (a) and (b) is represented by the calculated ΔE_f and ΔH_{cp}, respectively. Experimentally synthesized phases are marked with a black circle.

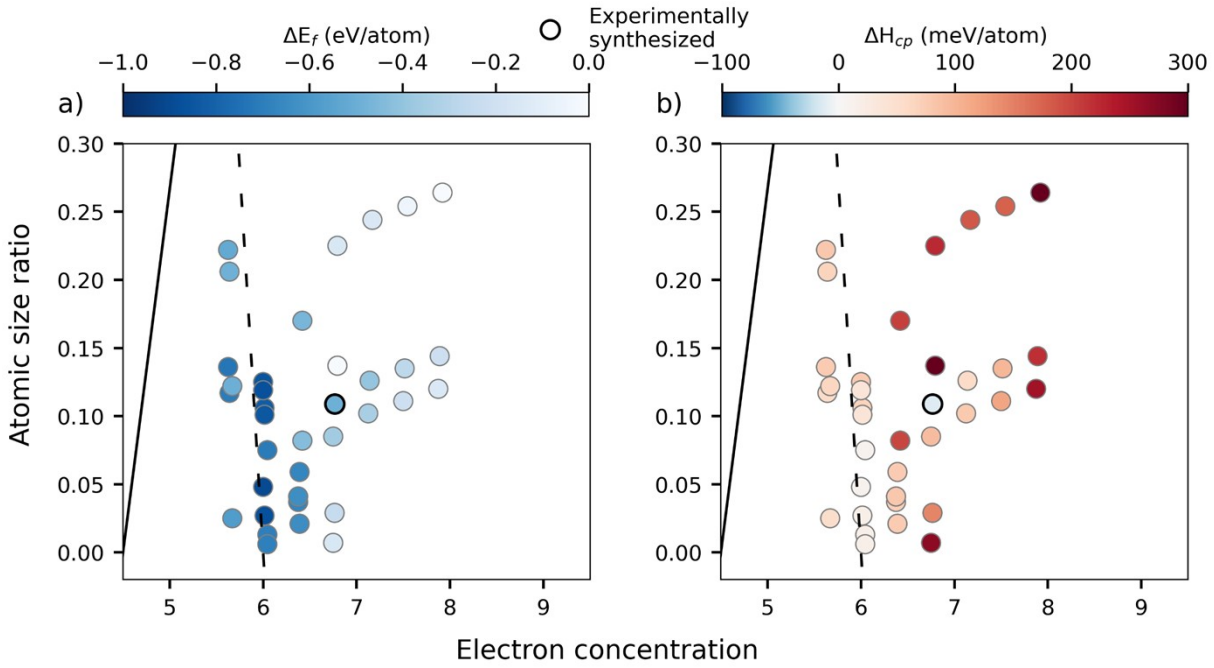

Figure S16. Atomic size ratio as a function of the electron concentration where each data point represents the lowest symmetry of a ^{M_3AB_4} phase. The solid black line refers to the stable regions of MAX phases considered in Ref. [5] and the dashed from Ref. [3] covering stable ^{M_2AB_2} compositions. All phases located to the left of the lines are supposedly stable. The colour gradient in (a) and (b) is represented by the calculated $^{\Delta E_f}$ and $^{\Delta H_{cp}}$, respectively. Experimentally synthesized phases are marked with a black circle.

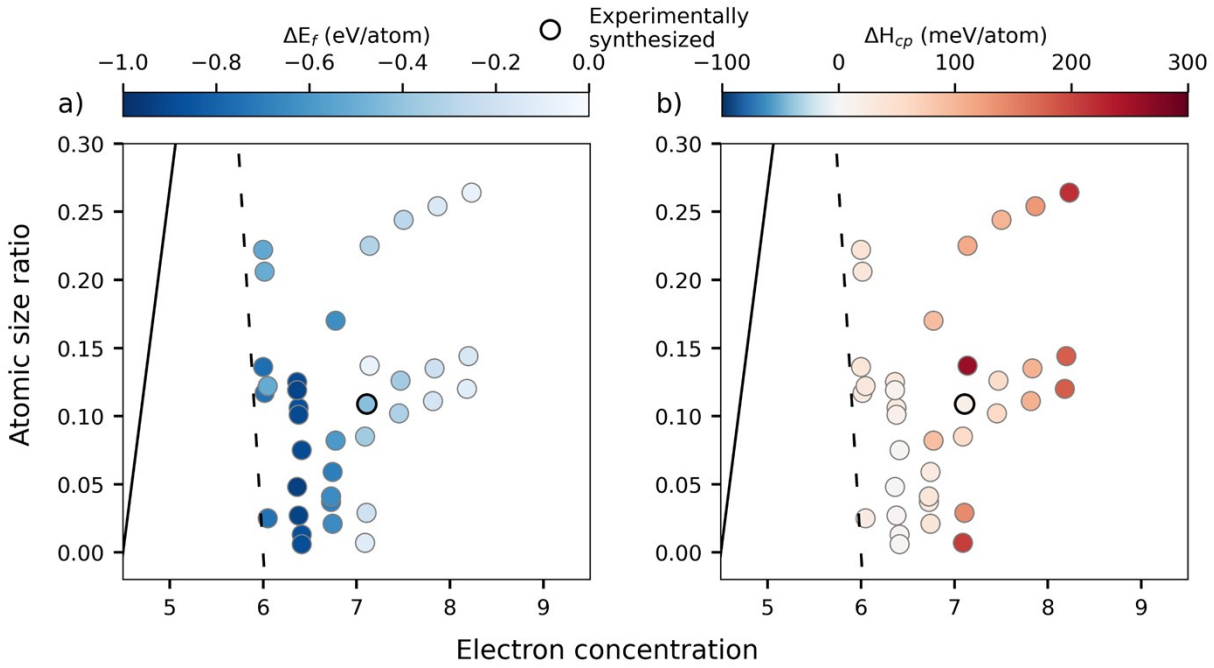

Figure S17. Atomic size ratio as a function of the electron concentration where each data point represents the lowest symmetry of a ^{M_4AB_6} phase. The solid black line refers to the stable regions of MAX phases considered in Ref. [5] and the dashed from Ref. [3] covering stable ^{M_2AB_2} compositions. All phases

located to the left of the lines are supposedly stable. The colour gradient in (a) and (b) is represented by the calculated $^{\Delta E_f}$ and $^{\Delta H_{cp}}$, respectively. Experimentally synthesized phases are marked with a black circle.

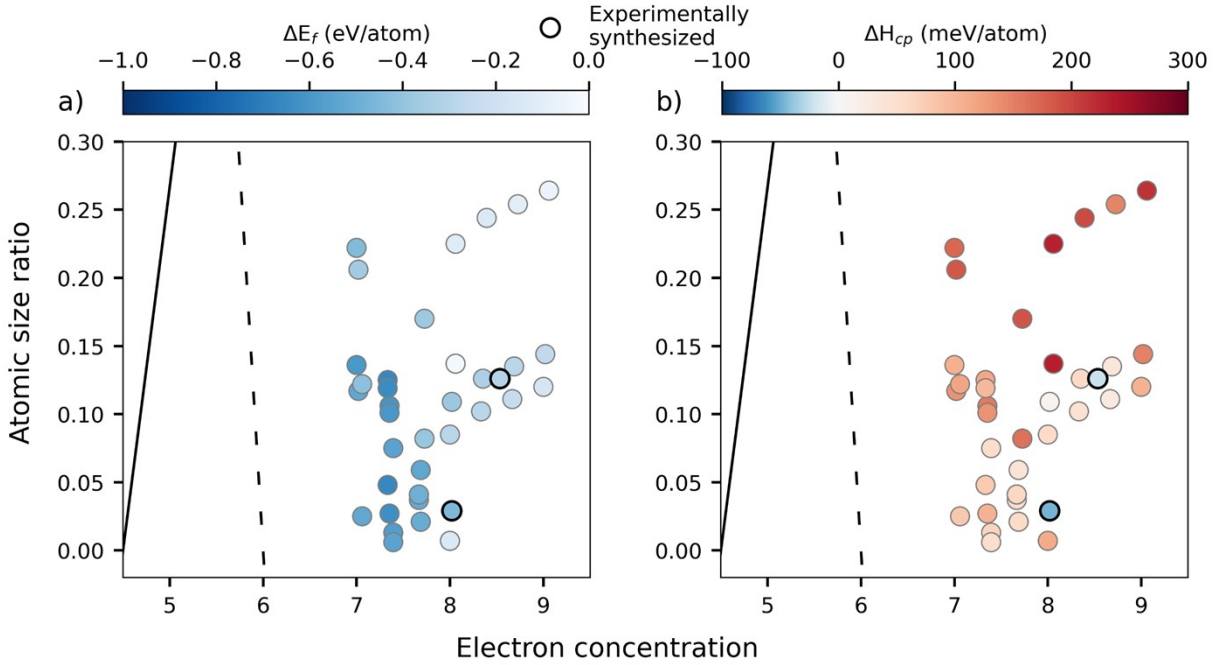

Figure S18. Atomic size ratio as a function of the electron concentration where each data point represents the lowest symmetry of a ^{MAB} phase. The solid black line refers to the stable regions of MAX phases considered in Ref. [5] and the dashed from Ref. [3] covering stable ^{M_2AB_2} compositions. All phases located to the left of the lines are supposedly stable. The colour gradient in (a) and (b) is represented by the calculated $^{\Delta E_f}$ and $^{\Delta H_{cp}}$, respectively. Experimentally synthesized phases are marked with a black circle.

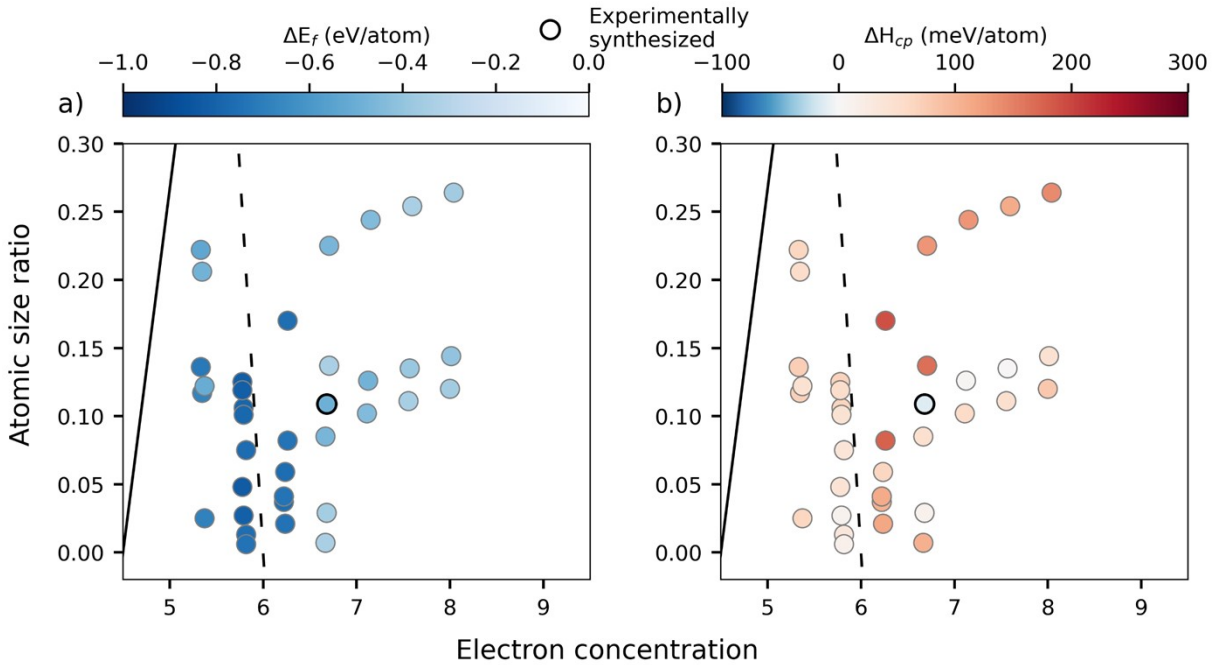

Figure S19. Atomic size ratio as a function of the electron concentration where each data point represents the lowest symmetry of a ^{M_4AB_4} phase. The solid black line refers to the stable regions of MAX phases

considered in Ref. [5] and the dashed from Ref. [3] covering stable M_2AB_2 compositions. All phases located to the left of the lines are supposedly stable. The colour gradient in (a) and (b) is represented by the calculated ΔE_f and ΔH_{cp}, respectively. Experimentally synthesized phases are marked with a black circle.

Supplementary references

1. Deskin, W.A., *Inorganic chemistry: Principles of structure and reactivity (Huheey, James E.).* Journal of Chemical Education, 1973. **50**(7): p. A379.
2. Greenwood, N.N. and A. Earnshaw, *Chemistry of the Elements 2nd Edition*. 1997.
3. Shen, C., et al., *Designing of magnetic MAB phases for energy applications.* Journal of Materials Chemistry A, 2021. **9**(13): p. 8805-8813.
4. Maintz, S., et al., *LOBSTER: A tool to extract chemical bonding from plane-wave based DFT.* Journal of Computational Chemistry, 2016. **37**(11): p. 1030-1035.
5. Zhang, Y., et al., *The role of Hume-Rothery's rules play in the MAX phases formability.* Materialia, 2020. **12**: p. 100810.